Characterization of the state of a droplet on a micro-textured silicon wafer using ultrasound

N. Saad, R. Dufour, Pierre Campistron, Georges Nassar, Julien Carlier, M. Harnois, B. Merheb, Rabah Boukherroub, V. Senez, J. Gao, et al.

Characterization of the state of a droplet on a micro-textured silicon wafer using ultrasound

Cite as: J. Appl. Phys. **112**, 104908 (2012); https://doi.org/10.1063/1.4767223
Submitted: 30 July 2012 • Accepted: 26 October 2012 • Published Online: 29 November 2012

N. Saad, R. Dufour, P. Campistron, et al.

Characterization of the state of a droplet on a micro-textured silicon wafer using ultrasound

N. Saad,[1,2] R. Dufour,[3,4] P. Campistron,[1] G. Nassar,[1] J. Carlier,[1] M. Harnois,[3] B. Merheb,[2] R. Boukherroub,[4] V. Senez,[3] J. Gao,[1] V. Thomy,[3] M. Ajaka,[2] and B. Nongaillard[1]
[1]*Université de Valenciennes et du Hainaut-Cambrésis, Institute of Electronics, Microelectronics and Nanotechnology (IEMN, UMR 8520), Le Mont Houy 59313, France*
[2]*LPA, EDST, Université Libanaise, P.O. Box 90656, Jdeidet, Lebanon*
[3]*University Lille Nord de France, Institute of Electronics, Microelectronics and Nanotechnology (IEMN, UMR 8520), Cité Scientifique, Avenue Poincaré, BP 60069, 59652 Villeneuve d'Ascq, France*
[4]*Interdisciplinary Research Institute (IRI, USR 3078), Parc de la Haute Borne, 50 Avenue de Halley, BP 70478, 59658 Villeneuve d'Ascq, France*

(Received 30 July 2012; accepted 26 October 2012; published online 29 November 2012)

In this work, we propose acoustic characterization as a new method to probe wetting states on a superhydrophobic surface. The analysis of the multiple reflections of a longitudinal acoustic wave from solid-liquid and solid-vapor interfaces enables to distinguish between the two well known Cassie-Baxter and Wenzel wetting configurations. The phenomenon is investigated experimentally on silicon micro-pillars superhydrophobic surfaces and numerically using a finite difference time domain method. Numerical calculations of reflection coefficients show a good agreement with experimental measurements, and the method appears as a promising alternative to optical measurement methods.
 [http://dx.doi.org/10.1063/1.4767223]

I. INTRODUCTION

Inspired by nature, superhydrophobic surfaces have been studied extensively during the last decade. These surfaces, displaying extremely low adhesion to water, exhibit self-cleaning and drag reduction properties which are of high interest for microfluidic and lab on chip applications. They are used, for instance, in nanosensors for the detection of attomolar concentrations of molecules,[1] in electrowetting based devices for the reduction of drops friction and biofouling,[2] or as templates for self-assembly of nanostructures.[3]

Superhydrophobic behaviour is usually achieved by associating low surface energy materials to micro or nanoscale roughness. Liquid repellency is then increased due to the fact that liquid drops stand on top of the roughness in a so-called Cassie-Baxter configuration, trapping air pockets between the asperities (Figure 1(a)). When an external force is applied to the drop, a transition is observed to another configuration referred to as Wenzel wetting state. In that case, liquid spreads and engulfs the surface topography (Figure 1(b)), resulting in a loss of repellency properties.

In order to find out the wetting configuration of a drop at rest on a superhydrophobic surface, different approaches are usually adopted.

On the one hand, the most common method consists in a macroscopic measurement of drop apparent contact angle θ^* and adhesion by mean of contact angle hysteresis (difference between advancing and receding apparent contact angles).[4,5] However, this approach does not provide accurate information on the local interface configuration below the drop and does not allow to distinguish composite states. Moreover recent studies demonstrated that apparent contact angles only depend on liquid-surface interaction in the vicinity of the contact line and consequently are not directly related to the liquid-solid interaction occurring below the drop.[6,7]

On the other hand, several optical methods have been developed to capture the interface configuration below the drop. Moulinet and Bartolo used reflection interference contrast microscopy (RICM) to monitor the Cassie-Wenzel transition of evaporating drops on pillared PDMS superhydrophobic surfaces.[8] Such optical characterization appears to be very accurate in resolving the composite interface configuration. However, it is limited to transparent surfaces only. Also, Rathgen and Mugele analysed diffraction patterns to capture the interface deformation on a superhydrophobic silicon surface made of rectangular grooves.[9] This method leads to a very accurate description of the liquid meniscus between surface asperities (uncertainty is a few nanometers) but requires a relatively complex setup (Ar-ion laser along with rotating glass container and photodiodes).

Wetting states can also be characterized using electrical methods particularly Tuberquia *et al.*[10] recently demonstrated the use of electrochemical impedance spectroscopy (EIS) to monitor Cassie to Wenzel transition on superhydrophobic polymethylene surfaces.

Ultrasound, beside acoustic (or low-frequency vibration methods), are commonly used to detect and characterize defects in high-performance composite structures[11] and to help highlighting adhesion levels.[12,13] These waves are also used to characterize the mechanical behaviour of solids and fluids to measure and to monitor a sample in a non-destructive way, hence their importance for surface and interface characterization.

In the field of acoustics, a first attempt to characterize wetting states on superhydrophobic surfaces was made by McHale and Roach *et al.*[14,15] They studied the effect of superhydrophobic coatings on the response of quartz crystal microbalance (QCM). They observed variations in the QCM resonance frequency related to a change of the boundary

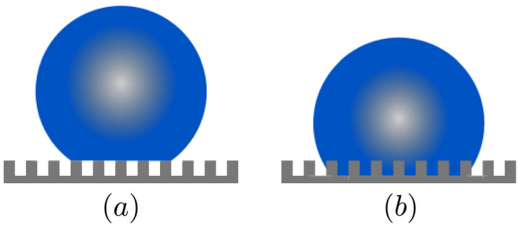

FIG. 1. (a) Cassie-Baxter and (b) Wenzel wetting regimes on a pillar based superhydrophobic surface.

conditions for shear forces depending on the wetting state of the liquid. This method consists in dipping the QCM resonator in the liquid medium and the superhydrophobic coating needs to be patterned directly on top of the sensor. Thereby it is not well suited to characterize the wetting state of droplets nor to be implemented in a microfluidic device.

We present in this paper an alternative acoustic method which consists in measuring the multiple reflections of ultrasound waves on a superhydrophobic silicon surface in contact with water. Contrary to the previous electrical or acoustic methods,[10,14,15] the approach enables to perform a more local measurement depending on the size of the transducer. It also enables potential implementation in microfluidic devices and is non invasive with respect to the liquid. Indeed no electrode or resonator needs to be immersed into the liquid to be characterized. Particularly, it makes it possible to characterize the wetting state of droplets, which offers an interesting perspective for real time monitoring of drop wetting state in digital microfluidic devices. Moreover, the acoustic sensor can be decoupled from the superhydrophobic surface. To our knowledge, this is the first time this method is used to characterize these interfaces.

The surfaces are silicon wafers composed on one side of superhydrophobic micro-pillars of well defined dimensions and on the other side of zinc oxide (ZnO) acoustic transducers. A finite difference time domain (FDTD) method enables the numerical calculation of acoustic reflection coefficients which were compared to experimental results. We were able to show that high frequency ultrasound is sensitive to the drop wetting state.

This paper is structured as follows. FDTD method is presented in Sec. II and numerical results in Sec. III. Section IV summarizes the microfabrication process used to obtain superhydrophobic surfaces and ZnO transducers. Then we present our measurement and data processing methods, and finally we compare experimental results to simulations.

II. COMPUTATIONAL MODEL

In the numerical approach, we use a two-dimensional model. The structures are assumed to be infinite along the Z direction and the X and Y Cartesian coordinates are finite (OXYZ). The geometry consists of three distinct regions (Figure 2). The first region is composed of anisotropic mono-crystalline silicon micro structures of width a, height h, and pitch b. The second region is composed of water and the third one of air. Densities ρ along with longitudinal and transverse velocities C_l and C_t for different materials are

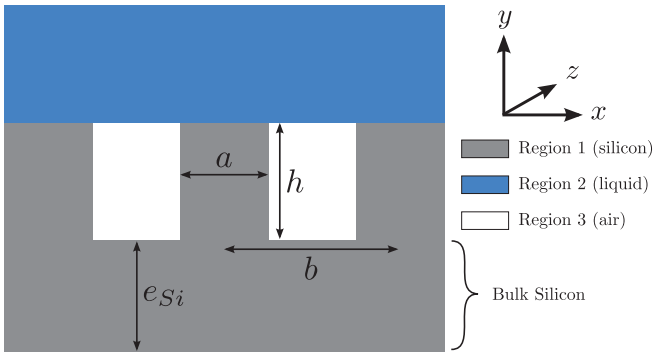

FIG. 2. Simulated micro pillar based superhydrophobic surface. The model is composed of 3 regions corresponding to monocrystalline [100] silicon, water, and air.

given in Table I. Silicon elastic constants are $c_{11} = 16.56 \times 10^{10}\,\mathrm{N\,m^{-2}}$, $c_{12} = 6.39 \times 10^{10}\,\mathrm{N\,m^{-2}}$, and $c_{44} = 7.95 \times 10^{10}\,\mathrm{N\,m^{-2}}$. It is to be noted that modeling of the acoustic wave reflection on such interfaces is difficult due to complex dispersion and diffraction phenomena occurring in the micro structures. Thereby no numerical model is totally accurate, and the approximation is more or less precise depending on the application.

As part of our work, a FDTD numerical model is developed to simulate the propagation and reflection of ultrasonic waves in elastic composites. It is to be noted that viscous effects are not taken into account and no-slip condition is assumed at the liquid-solid interface.

A. Mathematical model

In the following, we describe the mathematical model defining the equation of spatio-temporal sound wave propagation. The elastic wave equation is given by

$$\frac{\partial^2 u_i}{\partial t^2} = \frac{1}{\rho}.\frac{\partial \sigma_{ij}}{\partial x_j}. \tag{1}$$

In Eq. (1), u_i is the ith component of the displacement vector and σ_{ij} the stress tensor components. The latter can be written $\sigma_{ij} = c_{ijkl}.\frac{\partial u_l}{\partial x_k}$, where c_{ijkl} are the elastic constants. Since the system has translational symmetry along the z direction, the z component of the wave equation is decoupled from x and y components. The latter can be written as

$$\frac{\partial^2 u_x}{\partial t^2} = \frac{1}{\rho}.\left(\frac{\partial \sigma_{xx}}{\partial x} + \frac{\partial \sigma_{xy}}{\partial y}\right), \tag{2}$$

$$\frac{\partial^2 u_y}{\partial t^2} = \frac{1}{\rho}.\left(\frac{\partial \sigma_{xy}}{\partial x} + \frac{\partial \sigma_{yy}}{\partial y}\right). \tag{3}$$

TABLE I. Densities ρ, longitudinal velocity C_l, and transverse velocity C_t for the different regions considered in the numerical model.

Region	$\rho\,(\mathrm{kg\,m^{-3}})$	$C_l\,(\mathrm{m\,s^{-1}})$	$C_t\,(\mathrm{m\,s^{-1}})$
Silicon	2330	8433	5843
Water	1000	1490	0
Air	1.3	340	0

As the velocity is expressed by $\mathbf{v} = \frac{\partial \mathbf{u}}{\partial t}$, the above equations become

$$\frac{\partial v_x}{\partial t} = \frac{1}{\rho}.\left(\frac{\partial \sigma_{xx}}{\partial x} + \frac{\partial \sigma_{xy}}{\partial y}\right), \tag{4}$$

$$\frac{\partial v_y}{\partial t} = \frac{1}{\rho}.\left(\frac{\partial \sigma_{xy}}{\partial x} + \frac{\partial \sigma_{yy}}{\partial y}\right). \tag{5}$$

To compute the stress tensor, we used

$$\sigma_{xx}(t) = c_{11}\frac{\partial u_x(t)}{\partial x} + c_{12}\frac{\partial u_y(t)}{\partial y}, \tag{6}$$

$$\sigma_{yy}(t) = c_{11}\frac{\partial u_y(t)}{\partial y} + c_{12}\frac{\partial u_x(t)}{\partial x}, \tag{7}$$

$$\sigma_{xy}(t) = c_{44}\left(\frac{\partial u_x(t)}{\partial y} + \frac{\partial u_y(t)}{\partial x}\right). \tag{8}$$

B. Analytical equations

To develop the FDTD method, we have to transform the governing differential equations in the time domain into finite differences and solve them as small discrete time increments by iteration. To do so, the computational domain is divided into subdomains $i_{\max}, j_{\max}$ (grids), with dimensions dx, dy, and the displacement vector components discretized according to

$$u_l(i,j,k) = u_l(i\Delta x, j\Delta y, k\Delta t), \quad l = x, y, \tag{9}$$

along

$$1 \le i \le i_{\max}, \quad 1 \le j \le j_{\max}, \quad \text{and} \ \ k \ge 0. \tag{10}$$

Referring to Sigalas,[16] discretization of the above equations allows us to compute the stress tensor $(\sigma_{xx}, \sigma_{yy}, \sigma_{xy})$ at point (i, j) at $t(n+1)$

$$\sigma^n_{xx}(i,j) = c_{11}(i+1/2,j).\frac{u^n_x(i+1,j) - u^n_x(i,j)}{dx} + c_{12}(i+1/2,j).\frac{u^n_y(i,j) - u^n_y(i,j-1)}{dy}, \tag{11}$$

$$\sigma^n_{yy}(i,j) = c_{11}(i+1/2,j).\frac{u^n_y(i,j) - u^n_y(i,j-1)}{dy} + c_{12}(i+1/2,j).\frac{u^n_x(i+1,j) - u^n_x(i,j)}{dx}, \tag{12}$$

$$\sigma^n_{xy}(i,j) = c_{44}(i,j+1/2).\frac{u^n_x(i,j+1) - u^n_x(i,j)}{dy} + c_{44}(i,j+1/2).\frac{u^n_y(i,j) - u^n_y(i,j-1)}{dx}, \tag{13}$$

where

$$c_{11}(i+1/2,j) = \sqrt{c_{11}(i+1,j).c_{11}(i,j)}, \tag{14}$$

$$c_{12}(i+1/2,j) = \sqrt{c_{12}(i+1,j).c_{12}(i,j)}, \tag{15}$$

$$c_{44}(i,j+1/2) = \sqrt{c_{44}(i+1,j).c_{44}(i,j)}. \tag{16}$$

The discretized wave equations

$$\frac{v^{n+1}_x(i,j) - v^n_x(i,j)}{dt} = \frac{1}{\rho(i,j)}\left(.\frac{\sigma^n_{xx}(i,j) - \sigma^n_{xx}(i-1,j)}{dx} + \frac{\sigma^n_{xy}(i,j) - \sigma^n_{xy}(i,j-1)}{dy}\right), \tag{17}$$

$$\frac{v^{n+1}_y(i,j) - v^n_y(i,j)}{dt} = \frac{1}{\rho(i+1/2,j+1/2)}\left(\frac{\sigma^n_{xy}(i+1,j) - \sigma^n_{xy}(i,j)}{dx} + \frac{\sigma^n_{yy}(i,j+1) - \sigma^n_{yy}(i,j)}{dy}\right), \tag{18}$$

with

$$\rho(i+1/2,j+1/2) = \sqrt[4]{\rho(i,j).\rho(i+1,j).\rho(i,j+1).\rho(i+1,j+1)}. \tag{19}$$

It is important to note that the discretizing method proposed here provides second order central differences for the space derivatives for greater precision. The displacement field components u_x and u_y must always be centered in the space considered.

C. Propagation conditions

1. Initial conditions

The medium is assumed to be in equilibrium at time $t = 0$, i.e., the stress and velocity are zero throughout the medium.

$$u_x = u_y = 0,$$

$$v_x = v_y = 0,$$

$$\sigma_{xx} = 0,$$

$$\sigma_{yy} = 0,$$

$$\sigma_{xy} = 0.$$

2. Excitation source

The initial excitation is imposed by setting the stress values to a specific location and time. In our case, we imposed the values of the displacement field and velocity at points in the structure where the transducer was located. In order to reconstruct the signal module a sine wave and then a

cosine wave were generated. The functions generating the displacement field as a function of time are thus given by Eqs. (20) and (21).

$$u_x = 0;\ u_y = A\sin(\omega t);\ v_x = 0;\ v_y = A\omega\cos(\omega t), \quad (20)$$

$$u_x = 0;\ u_y = A\cos(\omega t);\ v_x = 0;\ v_y = -A\omega\sin(\omega t), \quad (21)$$

where $\omega = 2\pi f$, $f = 800$ MHz, and A is the displacement amplitude of the stimulus.

3. Boundary conditions

The assumptions of a no-slip condition at the liquid-solid interface and zero stress at the fluid-fluid interface allows us to consider the internal boundary conditions of continuity of displacement and stress vector at the silicon-water interfaces, as well as free internal conditions between silicon and air.

Absorbing boundary conditions are generally used at the borders of the computational space to avoid undesirable signals being reflected by these boundaries. Among a variety of absorbing boundary conditions which have been examined and used in the literature, the most common conditions are the Wall conditions.[17,18] In our work, we used the first order absorbing boundary conditions (Wall/ABC). The second order absorbing boundary conditions may provide better results but lead to a significant increase in CPU computation time and storage.

III. NUMERICAL RESULTS

All the calculations reported in this paper are for $dx = dy = 5 \times 10^{-7}$ m and $dt = 1.048 \times 10^{-11}$ s. Spatial sampling was chosen in such a way that decreasing its value would leads to $\approx 1\%$ variation in the results. dt was chosen to satisfy the Courant stability criterion (Eq. (22)).

$$dt \leq \frac{1}{C_{l,Si}\sqrt{\frac{1}{dx^2} + \frac{1}{dy^2}}}. \quad (22)$$

The results are given as the sum of the modulus, at each instant t, of a y-axis displacement u_y integrated on the sensor element.

Three geometries of micro structures were studied numerically, the dimensions of which are given in Table II. For all simulations, thickness e_{Si} of the bulk silicon between pillars and excitation source equals 396 μm. In the following, we first present several results considering the surface in contact with air only. This enables to assess the model validity by observing the evolution of time delays and amplitudes of acoustic echoes depending on the geometry of micro-structures. We then present numerical results considering the presence of water on the surface in order to demonstrate that this approach is sensitive to the wetting configuration (i.e., Cassie or Wenzel).

TABLE II. Geometries of the surfaces considered in the numerical simulations.

Geometry	a (μm)	b (μm)	h (μm)
A	15	30	20
B	15	30	40
C	30	45	20

A. Characterization of the structures without liquid

Considering geometry A, Figure 3(a) shows that the first echo occurs 94.3 ns after the signal emission, which matches the time for a wave to propagate through the medium. Indeed considering the propagation distance $d = 2e_{Si} = 792$ μm and the wave velocity in bulk silicon $C_{l,Si} = 8433$ m s^{-2}, the time delay t_1 for the first echo can be simply written $t_1 = d/C_{l,Si} = 93.9$ ns.

The second echo (Figure 3(b)) is then delayed by 4.4 ns by acoustic propagation in the micro-structures. In other words, the first echo corresponds to the reception of the wave signal reflected on the bottom of the space between pillars, and the second corresponds to the reception of the wave signal reflected on the top of the pillars. To compute the theoretical delay between the two echoes, we assume here that the wave velocity in the microstructures remains equal to $C_{l,Si}$, which remains a good approximation as far as a 2D model is concerned. Thereby the theoretical delay is $\Delta t = 2h/C_{l,Si} = 4.7$ ns, close to the value obtained from simulation.

To confirm this result, the same analysis was carried out for geometry B (Figure 3(c)). In that case the expected delay between the two echoes is $\Delta t = 9.5$ ns, still in close agreement with the numerical result (9.2 ns). This confirms that time spacing between echoes enables the height of the pillars to be evaluated.

The amplitude difference for the second echo between Figures 3(b) and 3(c) is related to mode conversions. When the incident longitudinal wave reaches the bottom part of the composite interface, it is partially converted into guided waves. Mode conversion is more significant as h is increased, resulting in a decrease of second echo amplitude in the case of higher structures.

In a second time, we compare the acoustic response of geometries A and C, which exhibit the same height $h = 20$ μm but different widths and pitches. For sample A, the fraction of reflecting surface at the bottom of the pillars is $\Phi^A_{bottom} = 1 - \frac{a}{b} = \frac{1}{2}$, while for sample C $\Phi^C_{bottom} = 1 - \frac{a}{b} = \frac{1}{3}$. The ratio between both values is $\frac{\Phi^A_{bottom}}{\Phi^C_{bottom}} = \frac{2}{3}$. In Figure 3(d), the same delay between the echoes is observed for the two samples, which is consistent since the delay only depends on the pillars height. However the amplitudes of the two echoes are different. As far as the first echo is concerned, the wave amplitude is larger for geometry A ($|U_y|^A_{max} = 11.6$ pm) compared to geometry C ($|U_y|^C_{\max} = 7.7$ pm). The reason is that the amplitude of the reflected echo is proportional to the variation of the reflecting surface. Considering the ratio between the two maximal amplitudes, we obtain $\frac{|U_y|^C_{\max}}{|U_y|^A_{\max}} \approx \frac{2}{3}$, which is equal to the aforementioned ratio of reflective surfaces $\frac{\Phi^A_{bottom}}{\Phi^C_{bottom}}$ at the bottom of the structures. Same

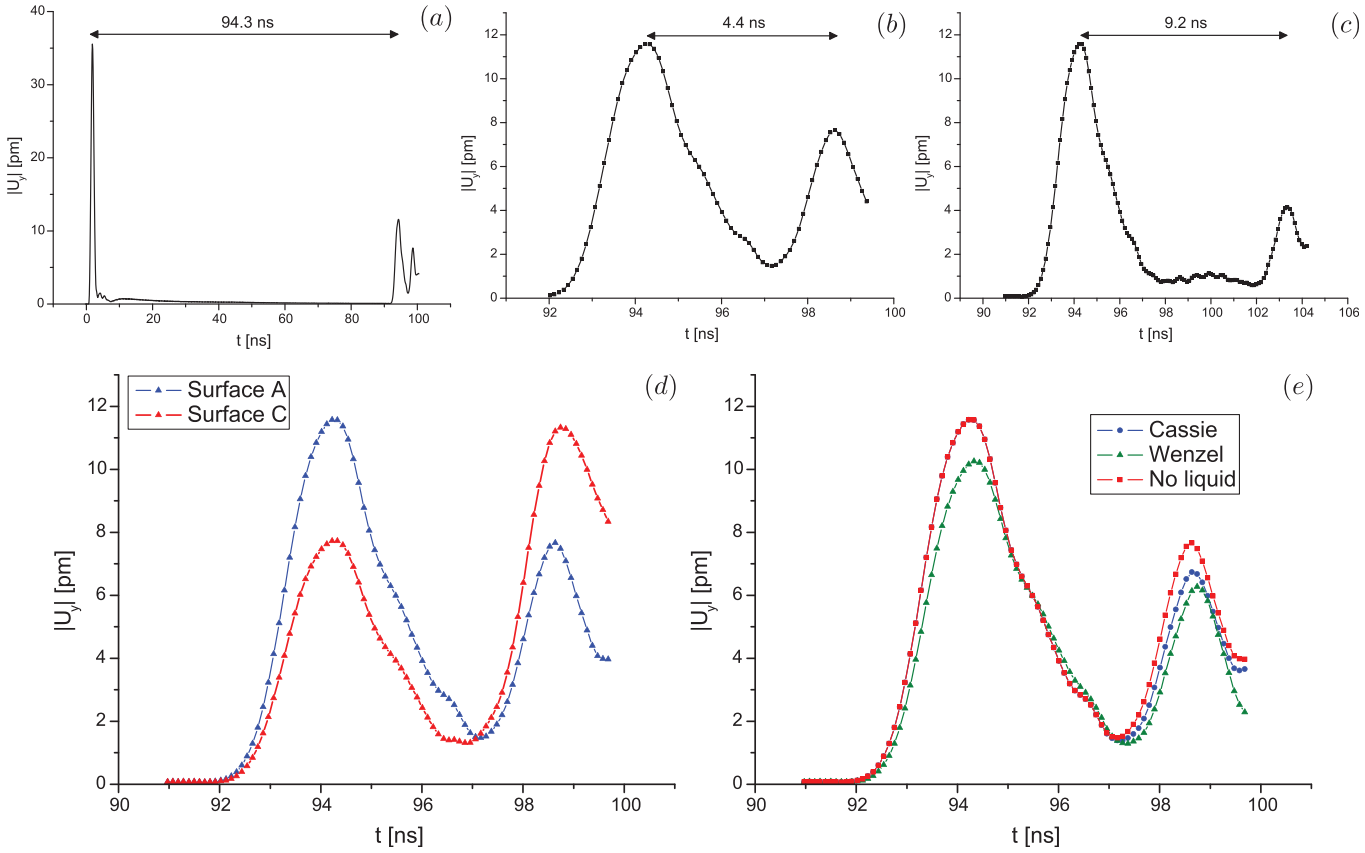

FIG. 3. Numerical results of acoustic wave amplitude. (a) Signal reflected on geometry A showing a delay of 94.3 ns between signal emission and first echo. (b) Time delay between the two echoes for $h = 20\ \mu$m. (c) Time delay between the two echoes for $h = 40\ \mu$m. (d) Influence of top and bottom surface areas on the reflected wave amplitudes (geometries A and C). (e) Influence of liquid penetration on the echoes amplitude: (red squares) *no liquid*, (blue circles) *Cassie* state, and (green triangles) *Wenzel* state. *No liquid* and *Cassie* cases overlap for the first echo.

reasoning is applied for the second echo, with a $\frac{3}{2}$ ratio observed between amplitudes of samples C and A (ratios between the fractions of top reflecting surfaces being complementary to the previous one).

B. Characterization of the structures in contact with liquid

In order to investigate the solid/fluid interaction, Wenzel and Cassie wetting states were considered and compared to the case of a surface exposed to air only. Figure 3(e) shows the results obtained on geometry A, for the three configurations (i.e., Cassie, Wenzel, and no liquid). Globally a decrease in the amplitude of echoes can be seen with the increase of liquid-solid contacting area. For the first reflected echo (still located at $t \approx 92$ ns after signal emission), the curve corresponding to the Cassie state (blue circles) superposes with the one obtained without liquid (dark squares). This is due to the fact that for the Cassie wetting regime, air is trapped between the pillars and consequently the reflection occurring at the bottom interface is not changed. However, for the Wenzel state (complete wetting, green triangles), the water soaks to the bottom of the pillars and acts as a coupling, which promotes the transmission and results in a decrease in the echo amplitude.

As far as the second echo is concerned, we notice a logical evolution of the amplitude depending on the configurations considered. When there is no liquid on the surface the reflection is maximal. Then in the Cassie configuration, solid-liquid contact occurs only on top of the pillars which reduces the reflection. Finally for the Wenzel configuration the whole pillar becomes wetted, as a consequence reflection is minimal. A simplistic approach considering pure vertical wave propagation in the pillars would result in an identical second echo amplitude for Cassie and Wenzel configurations (assuming that wave is reflected on top of the pillars only). However, as mentioned previously, guided waves appear in the pillars. As a consequence, reflection from the top of the pillars is influenced by wetted side-walls (Wenzel state) which lower the amplitude of the second acoustic echo.

IV. EXPERIMENTAL WORK

In this section, we first briefly review the fabrication process of superhydrophobic silicon surfaces and acoustic transducers. We then present the measurement method. The latter includes a calibration step which consists in measuring the acoustic response of the surface in air, then measurements are performed with the presence of a water drop on the surface. At last we focus on experimental results and show that analysis of the reflection coefficients on the composite interface enables to distinguish the different wetting states of a droplet.

It is to be noted that the model described previously along with simulation results consider two-dimensional patterns (i.e., infinite in the z direction), while the superhydrophobic surface used experimentally exhibits a three-dimensional

pattern of micro-pillars. For this reason it is not actually possible to quantitatively compare numerical and experimental acoustic responses. However, by first calibrating the measurement in air, it is possible to compare numerical and experimental values of normalized reflection coefficients at the top and bottom part of the composite interface (see Sec. IV B).

A. Microfabrication

The micro-structured surfaces in the present work were manufactured by the BioMEMS group at IEMN/University of Lille 1 on a $385 \pm 20\,\mu$m thick silicon wafer (Siltronix) ((100) oriented, single-side polished, phosphorus-doped, $0.009 - 0.01\,\Omega$cm resistivity). Fabrication process consists in a photolithography step followed by deep reactive ion etching (DRIE) of silicon and chemical surface functionalization with 1H,1H,2H,2H-Perfluorodecyltrichlorosilane. Only one micro-pillar geometry was investigated with the following dimensions: diameter $a = 15\,\mu\text{m} \pm 0.3\,\mu$m, height $h = 20\,\mu\text{m} \pm 0.3\,\mu$m, and pitch $b = 30\,\mu$m. A scanning electron microscopy (SEM) image of the micro-fabricated surface is shown in Figure 4.

Ultrasonic transducers were fabricated on the rear surface of the substrate and consist in the following stack: Pt (100 nm)/ZnO ($2.4\,\mu$m)/Pt (100 nm)/Ti (10 nm)/Si. The Ti/Pt ground electrode was first sputtered on the whole Si surface (intermediate Ti layer is added to improve Pt adhesion). Then ZnO piezoelectric and Pt top electrodes were deposited using a lift-off technique to obtain $250\,\mu$m in diameter transducers. The latter are able to generate 800 MHz longitudinal waves in the structure. Details concerning the fabrication process are reported in a previous work.[19]

B. Signal processing and measurement method

The experimental method is similar to the one used in a previous study.[20] Using this method we were able to characterize an unknown material with a controlled interface (smooth) and can thus characterize the interface of a known material (air, water). A scheme of measurement setup is represented in Figure 5. S_{11} scattering parameter (ratio of the complex amplitudes of the reflected and incident signals) is measured using a Suss Microtech probe coupled with a Hewlett Packard 8753 Vector Network Analyzer. This parameter can be written $S_{11}(f) = S_{11}^{el} + K.S_{11}^{ac}$, where S_{11}^{el} is the electrical term due to the reflection of the electrical wave on the transducer. $S_{11}^{el} = \frac{Z_t - 50}{Z_t + 50}$, with Z_t the electrical impedance of the transducer. K is the electro-acoustic conversion factor. S_{11}^{ac} is the acoustical term which represents acoustic wave propagation in silicon. The impulse response of the system was obtained by calculating the inverse Fourier transformation of parameter S_{11}. This response is composed of a series of echoes. As part of this study, we focus on the first echoes corresponding to waves that have made only one round trip through the silicon substrate. The working frequency is high enough so these echoes are time-resolved and diffraction phenomena are neglected.

The acoustic reflection coefficients at the bottom and upper part of the interface are respectively written r_1 and r_2 (Figure 5). These coefficients depend on the materials involved, the microstructures dimensions and the liquid wetting state. In order to express r_1 and r_2, we define the following parameters: S_t is the surface of the ultrasonic beam, S_p the projected pillar surface, S_h the complementary surface, S'_p the wetted surface of the pillars, and S'_h the wetted surface of the holes. We also define the following ratios: $\beta_p = S_p/S_t$, $1 - \beta_p = S_h/S_t$, $\beta_1 = S'_h/S_h$, and $\beta_2 = S'_p/S_p$. Moreover, coefficients corresponding to reflexion at a pure silicon-air or silicon-liquid interface are respectively written r_{Si/H_2O} and $r_{Si/air}$. r_1 and r_2 can be expressed as a function of the aforementioned parameters leading to Eq. (23).

$$r_1 = (1 - \beta_p).[\beta_1 r_{Si/H_2O} + (1 - \beta_1) r_{Si/air}], \tag{23}$$

$$r_2 = \beta_p.[\beta_2 r_{Si/H_2O} + (1 - \beta_2) r_{Si/air}]. \tag{24}$$

Because $r_{Si/air} = -1$, the above expressions can be reduced leading to

$$r_1 = (1 - \beta_p).[\beta_1 r_{Si/H_2O} - (1 - \beta_1)], \tag{25}$$

$$r_2 = \beta_p.[\beta_2 r_{Si/H_2O} - (1 - \beta_2)]. \tag{26}$$

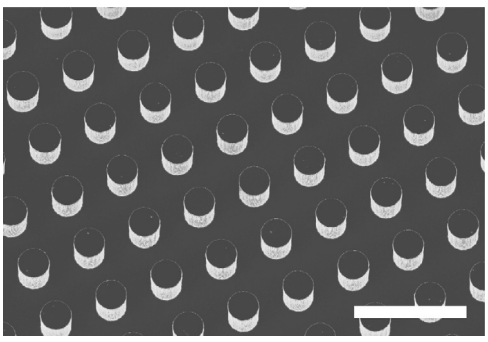

FIG. 4. SEM image of the microfabricated superhydrophobic silicon surface with dimensions $a = 15\,\mu$m, $h = 20\,\mu$m and $b = 30\,\mu$m. Scale bar equals $40\,\mu$m.

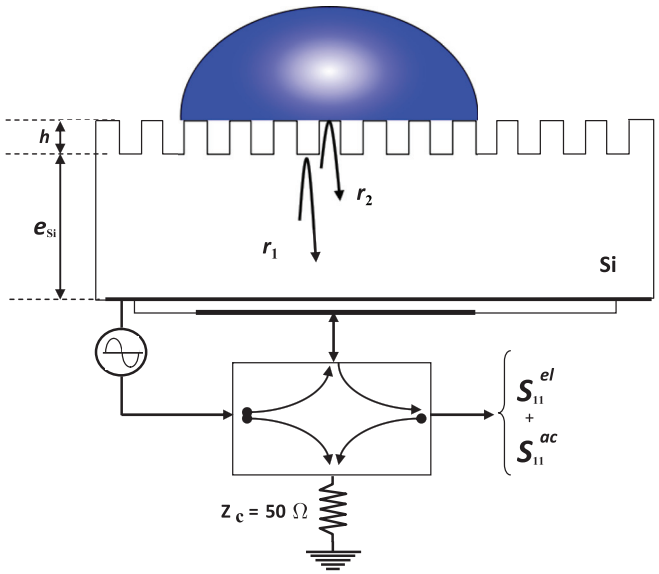

FIG. 5. Reflection of the acoustic waves at the micro-textured interface.

r_{Si/H_2O} is given by Eq. (27). It depends on silicon and water mechanical impedances $Z_{Si} = \rho_{Si}.C_{l,Si} = 19.6\,MRay$ and $Z_{H_2O} = \rho_{H_2O}.C_{l,H_2O} = 1.5MRay$, leading to $r_{Si/H_2O} = -0.86$.

$$r_{Si/H_2O} = \frac{Z_{H_2O} - Z_{Si}}{Z_{H_2O} + Z_{Si}}. \tag{27}$$

Regarding time delays between incident and reflected signals, the first echo of acoustic origin is expected to appear at instant $t_1 = 2e_{Si}/C_{l,Si}$ (round trip propagation in bulk silicon).

Concerning the time delay $\Delta t = t_2 - t_1$ between first and second acoustic echoes, the analytical expression is slightly different in the case of 3D structures. Indeed we previously considered $\Delta t = \frac{2h}{C_{l,Si}}$, assuming that propagation velocity in the 2D pillars remains equal to the longitudinal bulk silicon velocity (i.e., incident longitudinal wave is partially converted into guided waves as it reaches the bottom part of the structure, but it keeps propagating in the pillar with a group velocity close to $C_{l,Si}$). However in the case of 3D pillars, the wave is converted into a guided wave in the cylinder,[21,22] with a velocity C_g which can be considerably different from the bulk velocity $C_{l,Si}$. Thereby for the 3D geometry, time delay between signal emission and second acoustic echo is $t_2 = 2e_{Si}/C_{l,Si} + 2h/C_g$, and time delay between the two echoes is $\Delta t = 2h/C_g$.

According to previous works[21,22] and by averaging the guided wave velocity over the frequency band of the transducer (0.5–1.2 GHz), we estimated $C_g \approx 6024\ \mathrm{m\,s^{-2}}$.

Amplitudes of the two first echoes are $A_1 = |r_1 \Im^{-1}(K)|$ and $A_2 = |r_2 \Im^{-1}(K)|$. Because the conversion factor K is unknown, an initial calibration is carried out in air, in that case $\beta_1 = \beta_2 = 0$, leading to $r_1 = -(1 - \beta_p)$ and $r_2 = -\beta_p$. A_1^{air} and A_2^{air} are thus given by

$$A_1^{air} = |(1 - \beta_p)\Im^{-1}(K)|, \tag{28}$$

$$A_2^{air} = |\beta_p \Im^{-1}(K)|. \tag{29}$$

Following this calibration, measurements are performed for the surface in contact with water. Information regarding system status is given by the normalized coefficients r_i^* corresponding to the ratio A_i/A_i^{air}

$$r_1^* = \frac{A_1^i}{A_1^{air}} = |\beta_1 r_{Si/H_2O} - (1 - \beta_1)|, \tag{30}$$

$$r_2^* = \frac{A_2^i}{A_2^{air}} = |\beta_2 r_{Si/H_2O} - (1 - \beta_2)|. \tag{31}$$

r_{Si/H_2O} being known, r_1^* and r_2^* only depend on β_1 and β_2, in other words, on the liquid wetting state. For the Wenzel configuration $\beta_1 = \beta_2 = 1$, so the expected coefficients are $r_1^* = r_2^* = |r_{Si/H_2O}| = 0.86$. For the Cassie state $\beta_1 = 0$ and $\beta_2 = 1$, leading to theoretical values $r_1^* = 1$ and $r_2^* = |r_{Si/H_2O}| = 0.86$.

C. Experimental results

Experiments were performed using deionized water droplets. Following calibration with the surface exposed to air only, measurements were performed for the two main wetting states, i.e., Cassie and Wenzel configurations. In the first case the 1.2 μl drop is gently deposited on the surface and keeps a spherical shape (Figure 6(a)) which attests for the formation of a Cassie wetting state. Subsequently, the water drop is forced to spread between the micro-structures. The transition is experimentally induced by adding a slight trace of ethanol onto the surface prior to drop deposition. This locally reduces the interfacial energy and enables liquid penetration in the asperities. Macroscopically, a decrease in the contact angle along with an increase of drop spreading is observed as shown in Figure 6(b). It is to be noted that in both cases liquid covers the entire active surface of the transducer.

The acoustic response $S_{11}(t)$ for the three configuration (i.e., *no liquid*, *Cassie,* and *Wenzel*) is shown in Figure 7. The first echo occurs at $t_1 = 88.3$ ns after signal emission, and time delay between the two echoes is $t_2 - t_1 = 6.64$ ns. This corresponds to a bulk silicon thickness $e_{Si} = 372.3$ μm and to a pillar height $h = 19.8$ μm, in close agreement with the surface dimensions. As for the numerical simulations presented in Sec. III, amplitude of the first echo is similar for the *Cassie* and *no liquid* configurations, which attests for the homogeneous trapping of air pockets below the drop. Amplitude is clearly lowered for the *Wenzel* drop, demonstrating the presence of water between the pillars. As far as the second echo is concerned, the inset of Figure 7 shows that amplitude is gradually decreased from *no liquid* to *Wenzel* state because of the increasing liquid load on the pillars.

From these data are computed the normalized reflection coefficients r_1^* and r_2^* at the bottom and top of the pillars, respectively (averaged over 60 measurements, standard deviation is $\approx$0.01). They are represented on the histogram of Figure 8 for Cassie and Wenzel wetting states. First of all, the measured coefficient r_1^* at the bottom of the pillars for the Cassie configuration equals 1. This corresponds to the theoretical and simulated values ($r_{Si/air} = 1$) and is still coherent with homogeneous air trapping bellow the drop. Coefficient r_2^* corresponding to the pillars top is found equal to 0.85, which is in close agreement with the simulated value of 0.84 and with the fact that reflection occurs at a silicon-water interface with $|r_{Si/H_2O}| = 0.86$.

Concerning the Wenzel configuration, r_1^* clearly decreases reaching the value 0.85. This is coherent with the simulation results ($r_1 = 0.87$) and proves an homogeneous

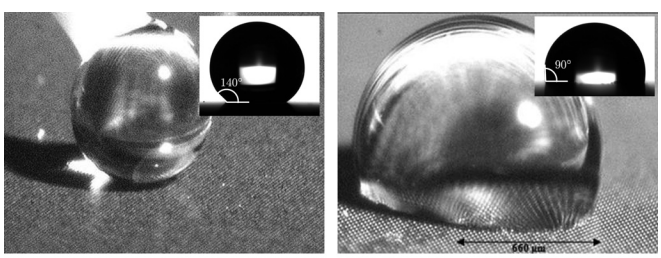

(a) (b)

FIG. 6. (a) Cassie and (b) Wenzel wetting states of a water drop on the microfabricated superhydrophobic silicon surface. Insets show lateral view obtained from a goniometer, apparent contact angles are, respectively, 140° and 90° for the Cassie and Wenzel drops.

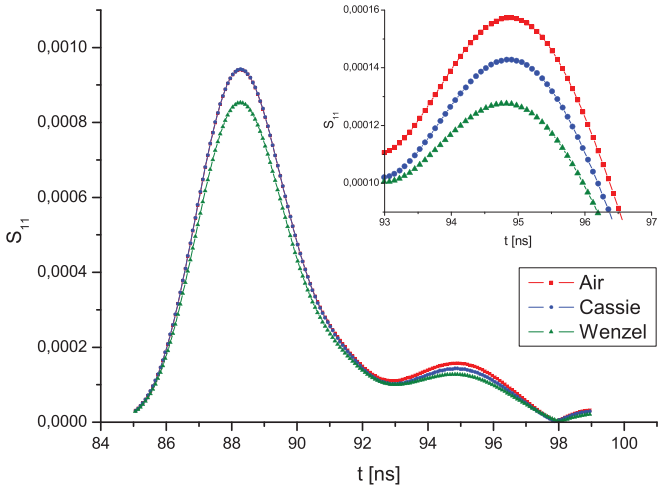

FIG. 7. Experimental reflected signal on the superhydrophobic silicon micropillars in the following configurations: (red squares) no liquid, (blue circles) Cassie state, and (green triangles) Wenzel state.

presence of liquid between the micro-pillars (partial filling of the asperities would have led to $0.86 < r_1^* < 1$). At the top of the pillars, measured $r_2^* = 0.75$ and simulated $r_2^* = 0.77$. These unexpected low values (lower than $r_{Si/H_2O} = 0.86$) could be explained by the particular behaviour of guided waves in the pillars.

As mentioned previously, the pillars having a sectional size comparable to the acoustic wavelength, a mode conversion occurs. Unlike longitudinal waves, the resulting guided waves are attenuated during propagation in the pillars (a simplified model shows that the amplitude is not homogeneous in the cross section of the pillar; consequently, the reflected amplitude is no more proportional to the area[23]). As far as Cassie state is concerned, such phenomena does not appear to strongly influence the normalized reflection coefficient at the top of the pillars (r_2^*, Figure 8) which remains close to theory. The reason is that, in the Cassie state, the pillars sidewalls consists of silicon-air interfaces, characterized by a

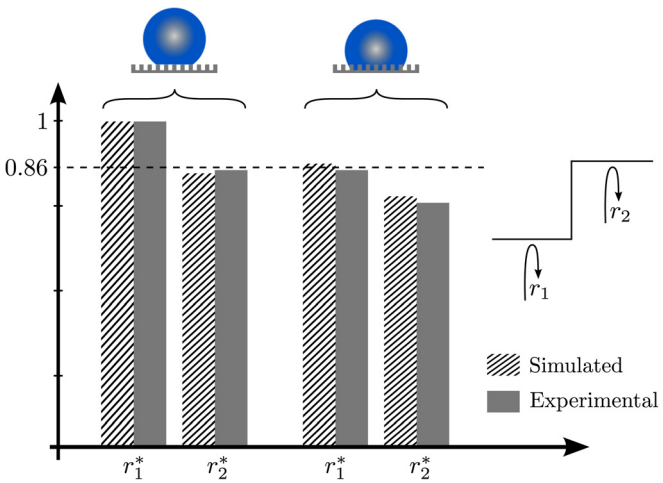

FIG. 8. Normalized reflection coefficients r_1^* and r_2^* at the bottom and top of the pillars, respectively, for Cassie and Wenzel wetting states. Horizontal dashed line corresponds to $|r_{Si/H_2O}| = 0.86$, which is the theoretical value for the reflection on a water interface.

reflection coefficient close to unity, which limits the attenuation phenomenon. On the other hand in the Wenzel configuration, pillars are surrounded by water. Because $|r_{Si/H_2O}| < 1$, attenuation is no more negligible, leading to a decrease of normalized coefficient r_2^* in Figure 8.

V. CONCLUSION

In this study, we investigated the potential of a new acoustic characterization method to probe wetting state of droplets on superhydrophobic surfaces.

Using a FDTD method developed for modelling acoustic propagation in 2D composite structures, we calculated the acoustic response and the reflection coefficients depending on the liquid wetting configuration (i.e., non wetting Cassie or penetrating Wenzel).

Experiments were performed using silicon micropillars based superhydrophobic surfaces. The results are in good agreement with theory and simulations, and the two extreme wetting configurations can be clearly distinguished by analysis of the acoustic reflection coefficients on the top and bottom part of the composite solid-liquid-vapor interface.

We have thus demonstrated that sound wave compression is a sensitive method for the characterization of the state of a liquid on a micro-textured surface. This approach presents several interesting perspectives such as the possibility to implement real time monitoring of wetting state in digital microfluidic devices involving superhydrophobic surfaces. It is non invasive in the sense that no electrode is needed in the liquid phase compared to electrochemical impedance measurement. Moreover it is well adapted to characterized droplet compared to previous acoustic method involving immersed sensors. Also, it is to be noted that the superhydrophobic surface can be uncoupled from the acoustic sensor, providing an acoustic matching layer in between.

Further studies will focus on the measurement of composite wetting state (for which liquid partially penetrates the superhydrophobic lattice) in order to monitor Cassie to Wenzel transitions.

ACKNOWLEDGMENTS

The Lebanese part of this study was supported by the Lebanese CNRS. The French part of the research was supported by the French CNRS. This work is supported by Nord-Pas-de-Calais Region through the 2008-2013 CIA State Region Planning contract and by the Ministry of Defense.

[1]F. De Angelis, F. Gentile, F. Mecarini, G. Das, M. Moretti, P. Candeloro, M. Coluccio, G. Cojoc, A. Accardo, C. Liberale, R. Zaccaria, G. Perozziello, L. Tirinato, A. Toma, G. Cuda, R. Cingolani, and E. Fabrizio, Nat. Photonics **5**, 682 (2011).
[2]F. Lapierre, G. Piret, H. Drobecq, O. Melnyk, Y. Coffinier, V. Thomy, and R. Boukherroub, Lab Chip **11**, 1620 (2011).
[3]B. Su, S. Wang, J. Ma, Y. Wu, X. Chen, Y. Song, and L. Jiang, Adv. Mater. **24**, 559 (2012).
[4]A. Marmur, Langmuir **20**, 3517 (2004).
[5]R. Dufour, M. Harnois, Y. Coffinier, V. Thomy, R. Boukherroub, and V. Senez, Langmuir **26**, 17242 (2010).

[6]L. Gao and T. J. McCarthy, Langmuir **25**, 14105 (2009).
[7]R. Dufour, M. Harnois, V. Thomy, R. Boukherroub, and V. Senez, Soft Matter **7**, 9380 (2011).
[8]S. Moulinet and D. Bartolo, Phys. J. E **24**, 251 (2007).
[9]H. Rathgen and F. Mugele, Faraday Discuss. **146**, 49 (2010).
[10]J. C. Tuberquia, W. S. Song, and G. K. Jennings, Anal. Chem. **83**, 6184 (2011).
[11]G. Rus, S. Wooh, and R. Gallego, IEEE Trans. Ultrason. Ferroelectr. Freq. Control **54**, 2139 (2007).
[12]L. Piche and D. Levesque, "High resolution ultrasonic interferometry for quantitative nondestructive characterization of interfacial adhesion in multilayer composites," Canadian patent 5,408,881 (1995). Assignee: National Research Council of Canada.
[13]D. D. Sukmana and I. Ihara, Adv. Technol. Mater. Process. J. **8**, 248 (2006), available at http://www.azom.com/article.aspx?ArticleID=3592.
[14]P. Roach, G. McHale, C. R. Evans, N. J. Shirtcliffe, and M. I. Newton, Langmuir **23**, 9823 (2007).
[15]G. McHale, P. Roach, C. Evans, N. Shirtcliffe, S. Elliott, and M. Newton, from the 2008 IEEE International Frequency Control Symposium, from the, Honolulu, Hawaii, 19-21 May 2008, pp. 698–704.
[16]*Photonic Crystals and Light Localization in the 21st Century*, edited by C. M. Soukoulis (Kluwer, 2009).
[17]A. Taflove and S. C. Hagness, *Computational Electrodynamics: The Finite Difference Time Domain Method* (Artech House, 1995).
[18]G. Mur, IEEE Trans. Electromagn. Compat. **EMC-23**, 377 (1981).
[19]S. Wang, P. Campistron, J. Carlier, D. Callens-Debavelaere, B. Nongaillard, A. N. Dieguene, G. Nassar, C. Soyer, and X. Zhao, IEEE Trans. Ultrason. Ferroelectr. Freq. Control **56**, 1483 (2009).
[20]P. Campistron, J. Carlier, N. Saad, J. Gao, M. Toubal, L. Dupont, G. Nassar, and B. Nongaillard, Adv. Mater. Res. **324**, 277 (2011).
[21]D. Bancroft, Phys. Rev. **59**, 588 (1941).
[22]J. Zemanek, Jr., J. Acoust. Soc. Am. **51**, 265 (1972).
[23]L. Pochhammer, J. Math. (Crelle) **81**, 324 (1876), available at http://gdz.sub.uni-goettingen.de/dms/load/img/.